metals

MDPI

Article

High Strain Rate and Stress-State-Dependent Martensite Transformation in AISI 304 at Low Temperatures

Lara Vivian Fricke [1,*], Gregory Gerstein [1], Andreas Kotzbauer [1], Bernd Breidenstein [2], Sebastian Barton [1] and Hans Jürgen Maier [1]

[1] Institute of Materials Science, Leibniz University Hannover, An der Universiät 2, 30823 Garbsen, Germany; gerstein@iw.uni-hannover.de (G.G.); andreas.kotzbauer@stud.uni-hannover.de (A.K.); barton@iw.uni-hannover.de (S.B.); maier@iw.uni-hannover.de (H.J.M.)

[2] Institute of Production Engineering and Machine Tools, Leibniz University Hannover, An der Universiät 2, 30823 Garbsen, Germany; breidenstein@ifw.uni-hannover.de

* Correspondence: fricke@iw.uni-hannover.de

Abstract: Deformation-induced martensitic transformation as the basis of a hardening process is dependent, among others, on the stress state. In applications such as cryogenic cutting, where a hardened martensitic subsurface can be produced in metastable austenitic steels, different stress states exist. Furthermore, cutting typically occurs at high strain rates greater than 10^3 s^{-1}. In order to gain a deeper insight into the behavior of a metastable austenitic steel (AISI 304) upon cryogenic cutting, the influence of high strain rates under different loading conditions was analyzed. It was observed that higher strain rates lead to a decrease in the α'-martensite content if exposed to tensile loads due to generated adiabatic heat. Furthermore, a lath-like α'-martensite was induced. Under shear stress, no suppression of α'-martensite formation by higher strain rates was found. A lath α'-martensite was formed, too. In the specimens that were subjected exclusively to compressive loading, almost no α'-martensite was present. The martensitic surface generated by cutting experiments showed deformation lines in which α'-martensite was formed in a wave-like shape. As for the shear specimens, more α'-martensite was formed with increasing strain rate, i.e., force. Additionally, magnetic etching proved to be an effective method to verify the transformation of ferromagnetic α'-martensite.

Keywords: high strain rates; deformation-induced martensitic transformation; cryogenic temperature; magnetic etching; subsurface hardening

Citation: Fricke, L.V.; Gerstein, G.; Kotzbauer, A.; Breidenstein, B.; Barton, S.; Maier, H.J. High Strain Rate and Stress-State-Dependent Martensite Transformation in AISI 304 at Low Temperatures. *Metals* **2022**, *12*, 747. https://doi.org/10.3390/met12050747

Academic Editors: Andrea Di Schino and Volodymyr A. Chernenko

Received: 20 January 2022
Accepted: 19 April 2022
Published: 27 April 2022

1. Introduction

Due to their low carbon content, conventional austenitic stainless steels cannot be hardened by rapid cooling. However, a hardened subsurface is advantageous to improve the wear resistance of a workpiece [1]. Processes other than heat treatment would be required to create a hardened subsurface for these steels. It would be of great use if a hardened subsurface could be created within the manufacturing process without any additional manufacturing step. Metastable austenitic microstructures have the ability to transform into martensite as soon as force is applied. The resulting deformation-induced martensite has an elevated resistance to hardness and wear [1].

Turning processes are often part of the machining of components and it is possible to create a hardened subsurface by cryogenic turning [1–7]. Reducing the temperature leads to a reduction in the stacking fault energy in the austenitic microstructure. This results in an enhanced transformation of austenite to martensite, and thus hardening of the steel [8,9]. However, turning uses very high strain rates. At low temperatures and high strain rates, the mechanical behavior of the material can differ significantly from the behavior at room temperature. The hardening behavior of materials is one of the most important pieces of information because understanding it is the first step to analyze and

evaluate manufacturing and structures. Hence, the correlation between the microstructure created by deformation-induced martensitic transformation (DIMT) and its mechanical behavior at high strain rates and low temperatures is of special interest.

Machining typically results in a strain rate between 10^3 and 10^6 s^{-1} [10]. Due to adiabatic heating of the specimen, high strain rates can lead to a reduction in strain hardening [11,12]. Therefore, at room temperature under tensile load, the DIMT is suppressed with increasing strain rate, which can be justified by the increase in adiabatic heat [13]. Hecker et al. also found that the temperature rise due to adiabatic heating at high strain rates is sufficient to lead to the suppression of martensitic transformation [14]. Moreover, Cao et al. found that with high strain rates, up to 10^3 s^{-1}, the temperature increase, compared to quasi-static tensile tests, was higher [12]. Thus, higher strain rates lead to an increase in the adiabatic heat created. The maximum martensitic volume fraction at strain rates above 10^3 s^{-1} is less than one fifth that at quasi-static strain rates (<0.2 s^{-1}) [12]. However, Eckner et al. also observed, among other aspects, the formation of deformation-induced martensite at strain rates above 10^5 s^{-1} [15].

Although the literature has demonstrated that the DIMT can result in substantial improvement in the mechanical properties, the effect cannot be exploited in turning processes yet, as the effects of strain rate and stress state in the actual process are not fully clear. In fact, within the complex cutting process, tensile, shear and compression forces act [16]. The objective of the present study was to shed light on the individual contributions to the DIMT. Thus, tensile, shear and compression experiments were designed to mimic the conditions in a cutting process and the data were correlated with microstructural analysis of the subsurface zones. Hereby, the aim was not quantitative analysis; however, the influence of the stress state on the general martensitic transformation mechanism was analyzed.

Comparable high strain rates to the cutting process cannot be achieved with conventional tensile and compression tests. Hopkinson developed a special test rig that allows loads to be exerted on specimens with a strain rate of 10^2 s^{-1} to 10^4 s^{-1} [17]. This so-called Split Hopkinson Bar consists of two concentrically aligned bars between which a specimen is clamped. The force is transmitted to the so-called incident bar via a projectile fired from a launcher. Here, exerting loads is possible in the directions of compression and tension [17,18]. In order to produce a larger amount of martensite and to analyze the influence of cryogenic temperature on the appearance of the martensitic microstructure, a cooling device was integrated into the experimental setup used in the present study, cf. Figure 1.

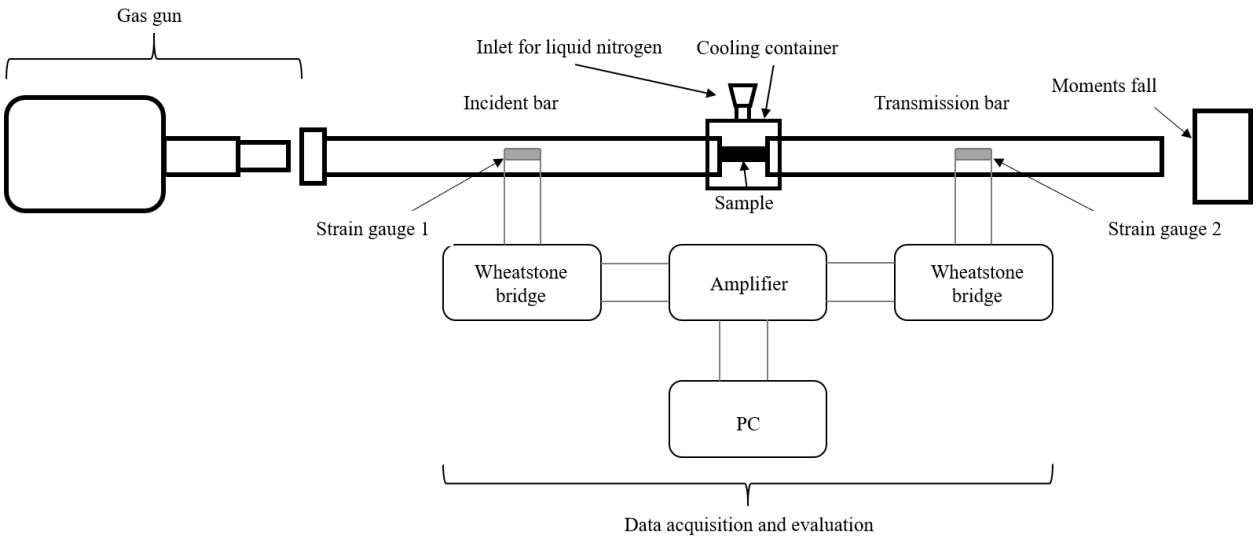

Figure 1. Drawing of the experimental setup of the compressive and cutting test; for the tensile test, the gas gun was positioned on the incident bar, cf. Figure 3c.

2. Materials and Methods

The experiments were performed using a metastable austenitic steel, AISI 304, which was solution-annealed at 1050 °C for 45 min and slowly cooled in the furnace to obtain a homogeneous microstructure. The measured alloy composition by spark spectroscopy was 0.028 wt.% C, 0.492 wt.% Si, 1.90 wt.% Mn, 18.24 wt.% Cr, 0.406 wt.% Mo, 7.95 wt.% Ni, 0.093 wt.% N and balance Fe.

In Figure 1, the setup of the Split Hopkinson Pressure Bar (SHPB) test is displayed. The SHPB apparatus consists of two long bars of 6061-T6 aluminium alloy, each two meters long and 18 mm in diameter. The specimens were placed between the two bars. On one side, a gas gun was mounted with a striker as the launcher. In Figure 2, the resulting spread of the waves inside the bars at the sample is shown. ε_I is the strain of the incident wave, ε_R of the reflected wave and ε_T the strain of the transmitted wave. v_1 is the speed of the incident bar and v_1 of the transmission bar. The strain rate of the specimen is calculated for the assumption that the specimen with the length L_S is in force equilibrium and is deforming uniformly ($\varepsilon_I + \varepsilon_R = \varepsilon_T$) with [18,19]:

$$\dot{\epsilon} = -2 \cdot \frac{C_B}{L_S} \cdot \epsilon_R \tag{1}$$

where C_B is the longitudinal wave speed of the bar. This type of equation is also called 1-wave analysis, since only the signal of the reflected wave is used to determine the strain rate [18–20].

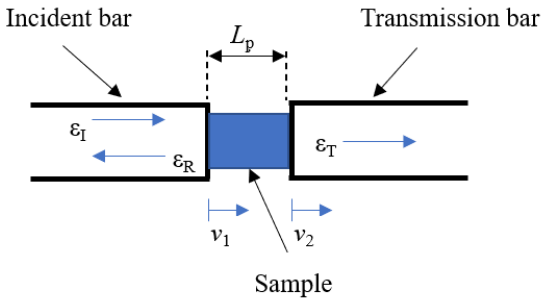

Figure 2. Schematic of the spread of the waves inside the bars.

The strain rates were measured using strain gauges attached to the incident and transmission bar; see Figure 1.

The impulse transmitted from the striker into the incident and transmission bars travels through the bars in the form of an elastic deformation. Strain gauges attached to the surface of the bar register the deformation and change their resistance according to the strain. The strain gauges were attached in the middle of the rods with a special adhesive. The strain gauges used (HBM, Darmstadt, Germany) had a k-factor of 2.03 and a resistance of 120 Ω. The resistance change of the strain gauge was conditioned by a Wheatstone half-bridge circuit and then combined and amplified in a measuring amplifier (ESA,110type SGA-0B/WB-SA, Olching, Germany). There, the strain gauge signals are added together. For evaluation of the strain rate, only the reflected wave (1-wave analysis; see Equation (1)) is needed. In case of the tensile tests and the shear tests, the specimen breaks, and thus the contribution from the transmitted wave to the overall signal is negligible. No stress values were determined. The strain gauge data were analyzed using a MatLab (Version Release 2021b, MathWorks Inc., Natick, MA, USA) script developed by [20]. A measurement gain of 1000 was chosen so that the resulting output voltage was in the range of 1 V to 10 V. The sampling rate was set to 1 MHz.

The Split Hopkinson tests conducted in this study were carried out with four different specimen geometries to simulate different stress states. The experimental setups are displayed in Figure 3. First, cutting specimens—see Figure 3a—and compression

specimens—see Figure 3b—were tested using the SHPB; see the experimental set-up in Figure 1. The cutting specimens were adapted to the experimental setup to simulate a turning process, similar to earlier studies [21,22]. The clamping consisted of a cutting holder attached to the transmission bar. Two turning tools were fixed in the clamping. The specimen was pushed through the blades of the turning tools by the momentum of the striker, which chipped the surface of the specimen, cf. Figure 3a.The newly created surface was analyzed by creating metallographic cross-sections.

The pressure sample was placed into a centered bore hole on the incident bar. To determine the influence of strain rate and temperature on the material properties of the specimens, two different impact speeds and sample temperatures were examined. Three samples were tested for each of the possible combinations. The whole fracture areas of the pressure samples were analyzed by metallographic cross-sections and two different etching methods.

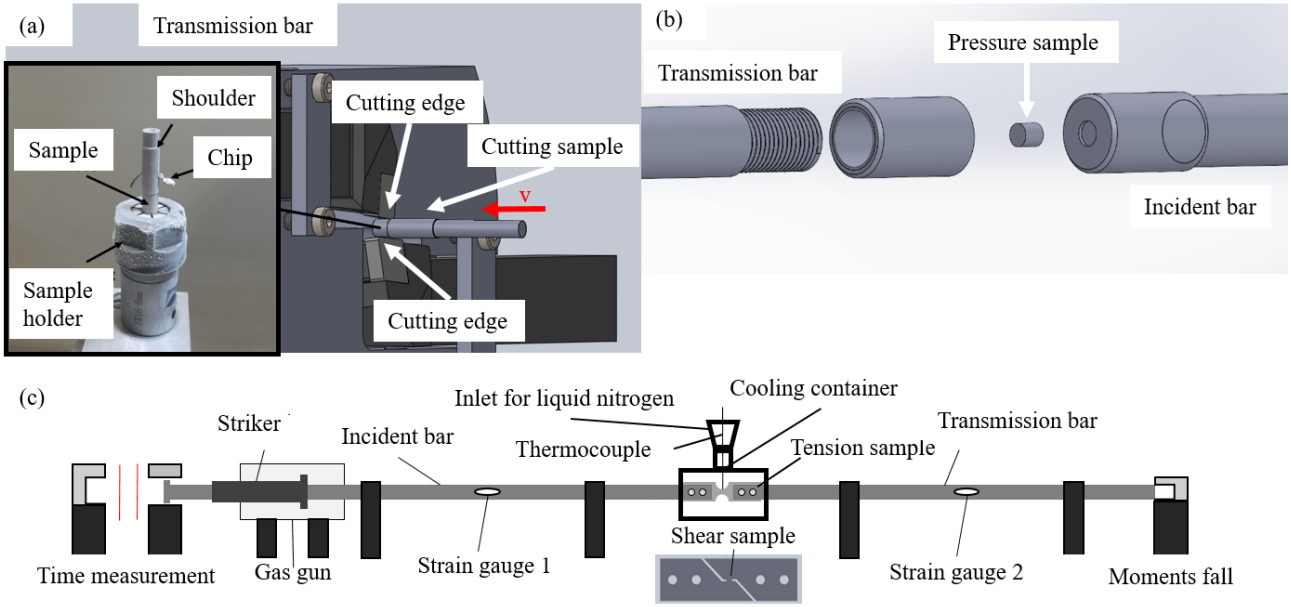

Figure 3. Clamped samples: (**a**) cutting experiment, (**b**) compressive test, (**c**) tensile/shear test.

In Figure 4, we provide an example of a compressive sample of (a) strain rate measured over time and (b) a shear test and (c) a tensile test. The average and maximum strain rate, as well as the maximum stress, are provided on each micrograph to correlate it to the martensite microstructure.

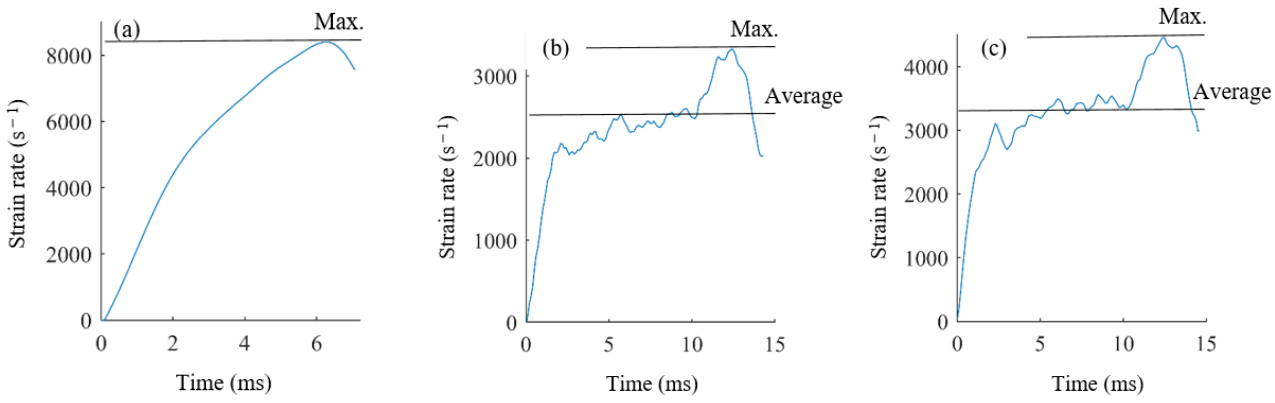

Figure 4. (**a**) Example of the strain rate vs. time in a compression test, (**b**) example of the strain rate vs. time during a shear test and (**c**) example of the strain rate vs. time during a tensile test.

The temperature of the compressive samples could not be measured directly in the process. Instead, a cooling curve was created with a reference sample, as described in [23]. A hole with a diameter of 1.5 mm and a depth of 3 mm was drilled into the surface of the sample. A thermocouple was used to measure the temperature during the cooling process.

To cool the cutting samples, they were immersed in liquid nitrogen in the clamped state for a defined time. The time required was again determined using a reference sample with a thermocouple; see Figure 5.

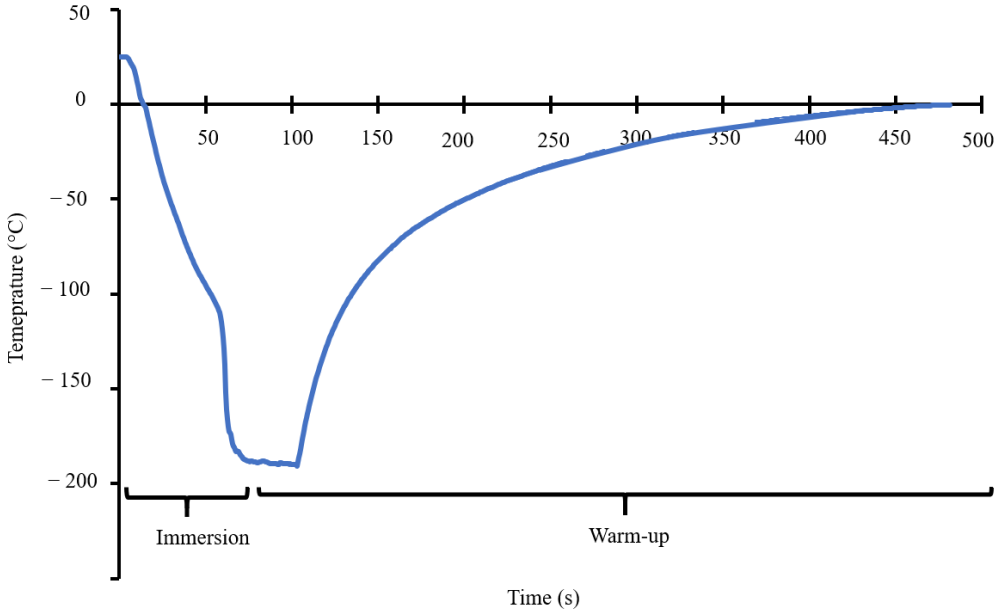

Figure 5. Temperature–time course during a cutting experiment; the sample was immersed in liquid nitrogen and then placed in the sample holder and the experiment was started once the given temperature was obtained; see main text for details.

Tensile and shear specimens were tested on the Split Hopkinson Tensile Bar (SHTB) test rig. Therefore, the Split Hopkinson test setup had to be modified; see Figure 3c. The gas gun was placed on one of the bars and accelerated a striker. The details of the striker are shown in Figure 3c. The striker for the tensile and shear experiments had a T shape to stroke an anvil attached to the end of the incident bar, pulling the incident bar along with it. The shear samples were designed according to a modified sample geometry of ASTM B831-05 designed by Merklein and Biasutti [24], cf. Figure 3c. To cool the samples to the desired temperature, liquid nitrogen was filled through the opening at the top of the cooling device. The temperature of the samples was controlled by a thermocouple. In Figure 6, high-speed photos of a tensile, shear and cutting specimen during the tests are shown.The fractured areas were analyzed with metallographic cross-sections and two different etching methods.

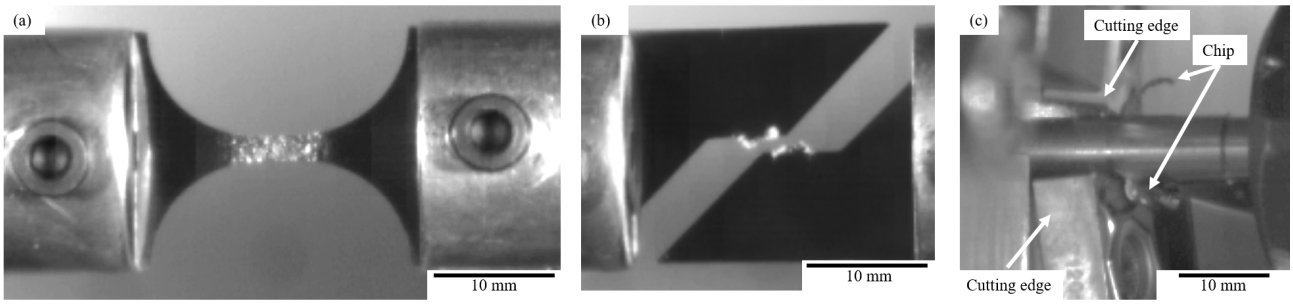

Figure 6. Pictures taken by a high-speed camera during the experiment: (**a**) tensile test, (**b**) shear test, (**c**) cutting test.

After testing, the microstructures of the samples were analyzed. For this purpose, the samples were ground with 2500-grit SiC abrasive paper and then polished with 1 µm diamond particles. Additionally, the samples were oxide-polished using Eposil M-11 by *QATM*, Mammelzen, Germany. After polishing of the samples, Beraha II color etchant (distilled water, hydrochloric acid, ammonium hydrogen difluoride) was applied, and images were captured with a Leica DM4000M microscope, Wetzlar, Germany. The samples for the SEM were etched using a V2A stain. A Scanning Electron Microscope (SEM, Zeiss Supra 55VP, Oberkochen, Germany) was used for Electron Backscatter Diffraction (EBSD) and Schmid factor analysis. For EBSD work, a beam energy of 20 kV was used. The step size used for EBSD mapping was 0.51 µm.

Although EBSD was successfully used for Schmid factor analysis in non-transformed grains, it was not suitable to quantify the martensite content or analyze the finer martensitic structure in these highly strained areas. In another study [7], however, it was possible to detect a bcc structure (a_0 = 2.866 Å) in small amounts even in the highly deformed areas. Olson and Cohen also described the strain-induced martensitic transformation as a fcc $\rightarrow$ bcc transformation. Further details of the transformation mechanism and the martensite structure can be found in Refs. [8,25]. Similarly, X-ray diffraction analysis of the thin surface layers on the small samples employed in the present study resulted in inconclusive data. Magnetic etching is another technique to probe the presence of ferromagnetic phases, which, in the current context, is the α'-martensite. Although magnetic etching is not very common in the literature, it can probe large areas, and reveals the fine martensitic microstructures. The magnetic etching was conducted by placing a polished sample on a permanent magnet and applying a ferrofluid (particle size 1 nm, type 157M-FER-10) containing ferromagnetic particles. The ferromagnetic particles align with the ferromagnetic parts of the samples under study so that the structure of the α'-martensite can be revealed [26]. As described by Talonen et al. [27], some uncertainties result when using magnetic etching to determine quantitative α'-martensite values. This is why the obtained contents in this study were qualitatively compared and are not stated here. Additionally, only the ferromagnetic α'-martensite phase can be detected. ϵ-martensite is paramagnetic and cannot be analyzed using magnetic etching. Although the formation of ϵ-martensite is likely to happen in this steel [6,28,29], the detectable α'-martensite often forms via the $\gamma \rightarrow \epsilon \rightarrow \alpha'$ mechanism [28]. As it is the latter that is of interest with respect to enhancing the mechanical properties, only the α'-martensite is considered in the following.

3. Results

In Figure 7, the microstructures of three tensile samples tested at −190 °C under different strain rates are displayed. The samples were etched using Beraha II. The fracture is located on the left side of the sample. The deformation and strain rate have the highest values at the point of the fracture that approaches the tip and decrease towards the opposite end [30]. In the black-colored areas, martensite is present. Colored areas are austenitic. However, using Beraha II, martensite cannot be quantitatively distinguished

from dislocations or twins. Thus, the effects of strain rate and stress state on martensite evolution were only qualitatively evaluated.

The analysis of the microstructure of two shear samples is displayed in Figure 8. In order to distinguish α'-martensite from other deformation structures, the samples were magnetically etched. It can be seen that despite a test temperature of −190 °C, only a few martensite spots are found on tip of the samples where the greatest deformation has occurred. Figure 8d shows a photograph of a shear specimen tested at a higher strain rate. Here, more brown areas and thus α'-martensite are seen.

Figure 9 shows an example of the fractured area of a compression specimen. In (a), the sample was etched with Beraha II. Many black areas, especially at the edges, where the strongest deformation occurred, are evident. However, magnetic etching reveals only a few α'-martensitic areas, cf. Figure 9b,c. The samples show the presence of blocky and lath-like α'-martensite.

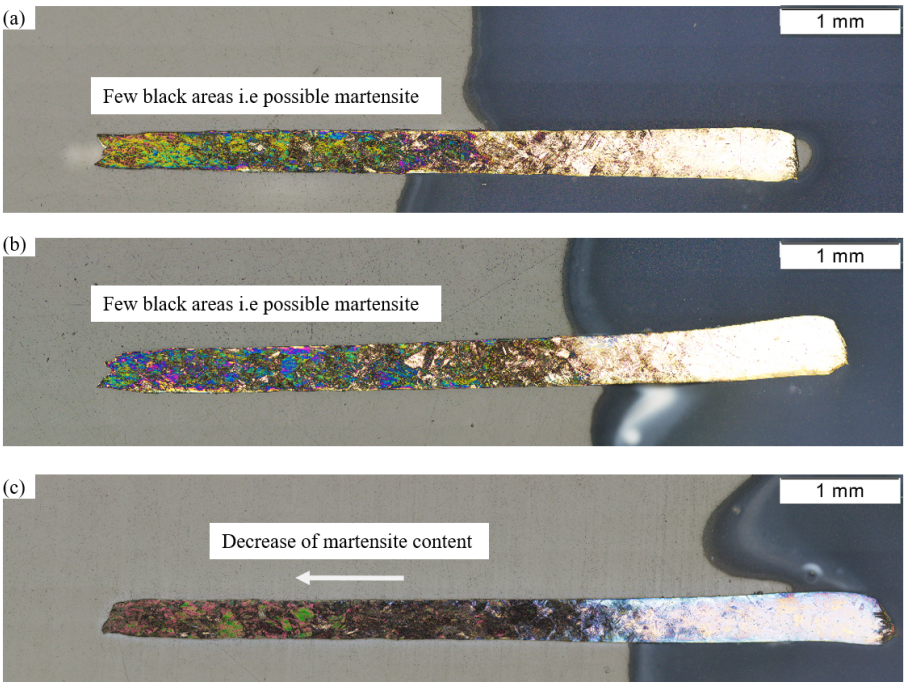

Maximum strain rate: 4.5 x 10^3 s^{-1}
Average strain rate: 3 x 10^3 s^{-1}

Maximum strain rate: 4 x 10^3 s^{-1}
Average strain rate: 3 x 10^3 s^{-1}

Maximum strain rate: 2.5 x 10^3 s^{-1}
Average strain rate: 1.7 x 10^3 s^{-1}

Figure 7. Microstructure after a Split Hopkinson tensile test at −190 °C for different strain rates, (**a**–**c**) from high to low; the samples were etched using Beraha II.

Maximum strain rate: 3 x 10^3 s^{-1}
Average strain rate: 2 x 10^3 s^{-1}

Maximum strain rate: 4 x 10^3 s^{-1}
Average strain rate: 3 x 10^3 s^{-1}

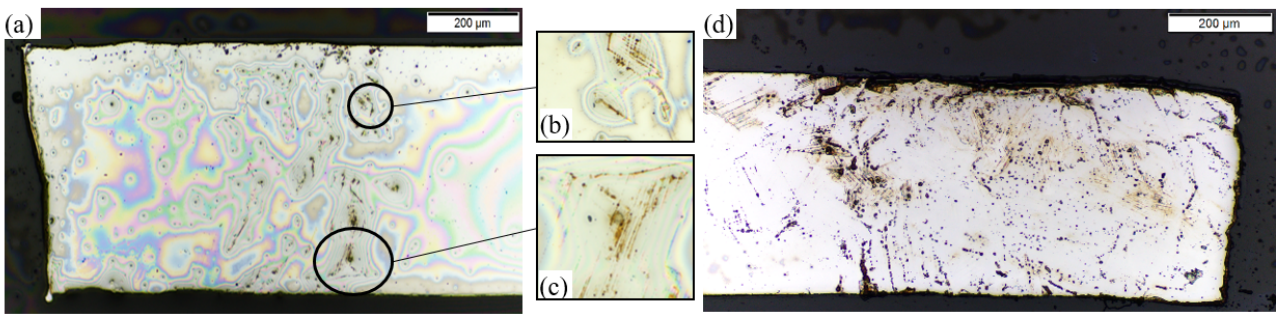

Figure 8. Microstructural analysis of a shear specimen tested at −190 °C: (**a**) magnetic etching, (**b**,**c**) lath martensite, (**d**) magnetic etching of a sample subjected to a higher strain rate.

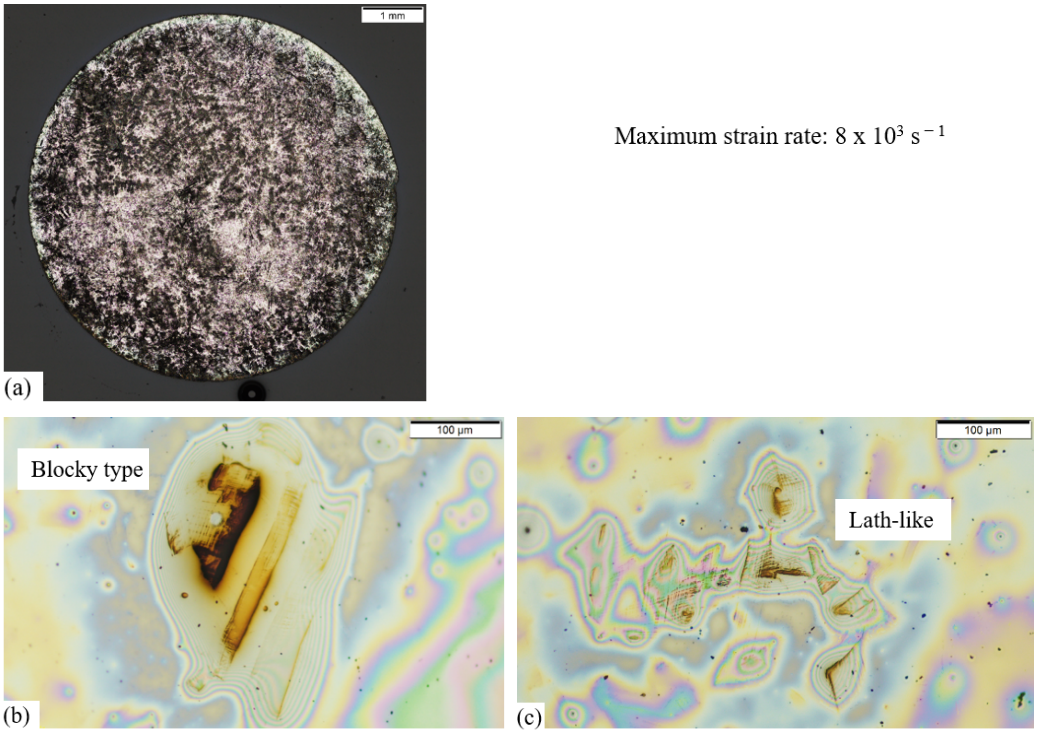

Figure 9. Microstructure analysis of the fracture area of a compression specimen tested at −190 °C: (**a**) Beraha II etching, (**b**) blocky martensite, (**c**) lath martensite.

Figure 10 shows the subsurface of a sample of the cutting experiment at room temperature. In the center of Figure 10a, a non-transformed area is visible. Magnetic etching and SEM both revealed that no α'-martensite or other deformation products were formed there, cf. Figure 10b,c.

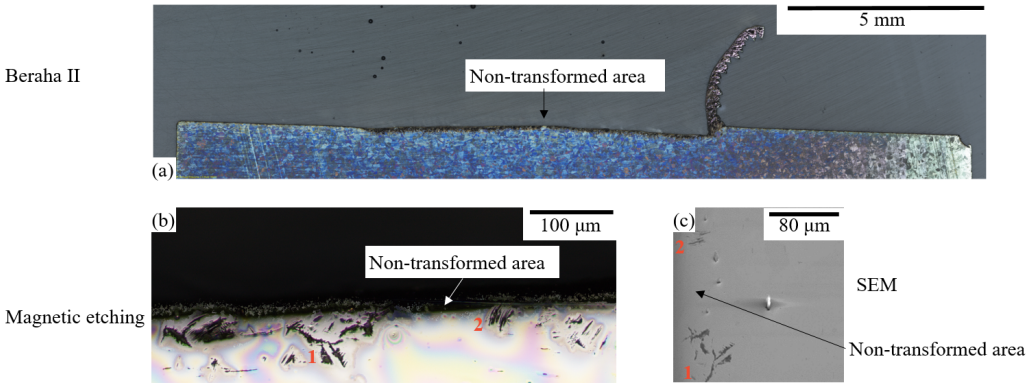

Figure 10. Microstructure analysis of specimen cut at room temperature: (**a**) Beraha II etching—a non-transformed grain (which is not black) is clearly visible, (**b**) magnetic etching, (**c**) SEM picture of the non-transformed grain for EBSD from (**a**,**b**). The regions labeled 1 and 2 mark the same areas in the different images.

A Schmid factor analysis showed that the non-transformed area was located within one grain. This grain had a low Schmid factor, cf. Figure 11b. The grain average misorientation (GAM) in Figure 11c shows the misorientation in an angle range of 1–7.5°. The GAM can be used to analyze possible subgrain developments or grain rotations.

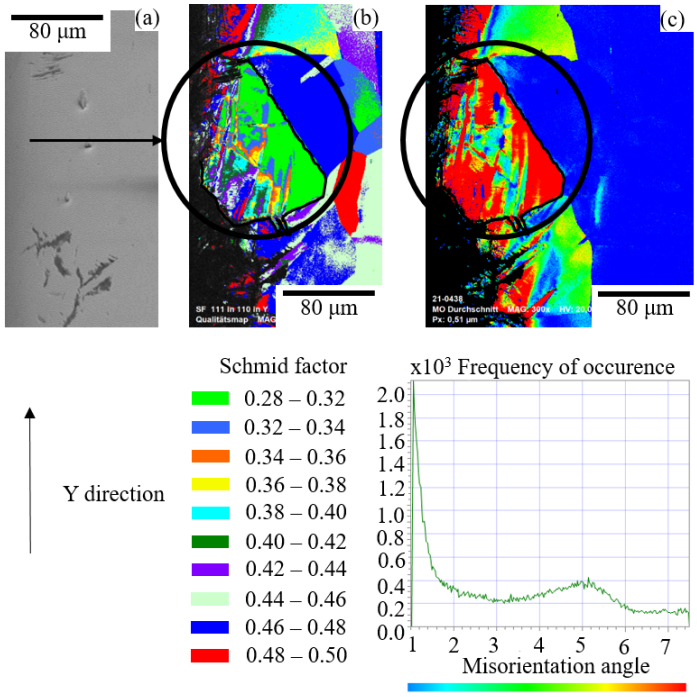

Figure 11. EBSD analysis of a specimen cut at room temperature: (**a**) SEM picture, (**b**) Schmid factor analysis of a non-transformed grain in Y direction for <111> in {110} and (**c**) GAM for 1–7.5° misorientaion angle.

On the other hand, the Schmid factor analysis for another non-transformed grain at a significantly lower temperature, −110 °C, was close to 0.5, cf. Figure 12a.

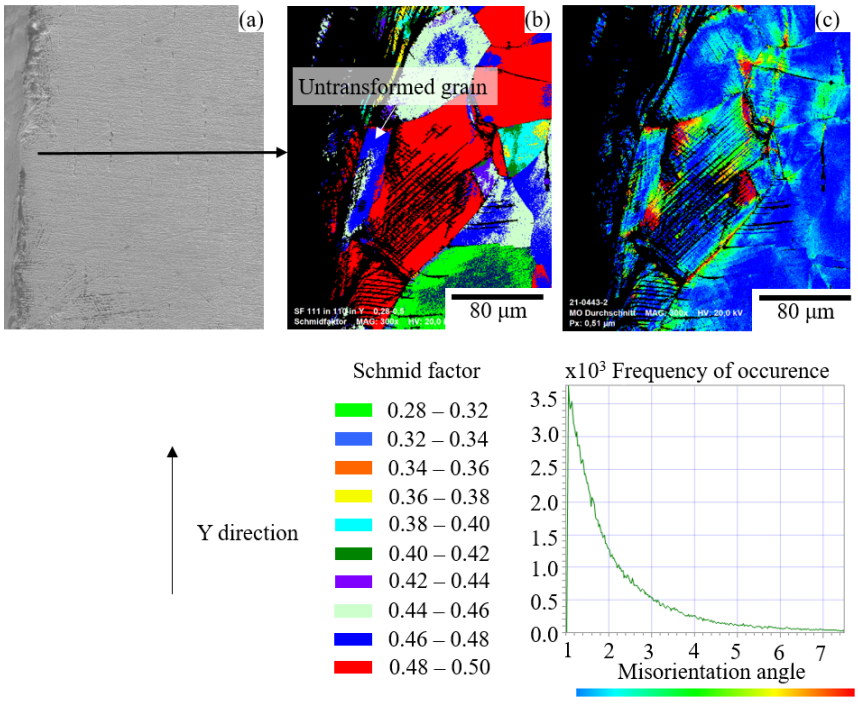

Figure 12. EBSD analysis of a specimen cut at −110 °C: (**a**) SEM picture, (**b**) Schmid factor analysis of a non-transformed grain in Y direction for <111> in {110} and (**c**) GAM for 1–7.5° misorientation angle.

A sample tested at −110 °C in the cutting experiment is shown in Figure 13. In Figure 13a, a picture of a sample etched with Beraha II is shown. In Figure 13b, a wave-like

shape of the α'-martensite is evident. In Figure 13c, a blocky α'-martensite is found just below the surface. With increasing depth, a lath-like α'-martensite was observed.

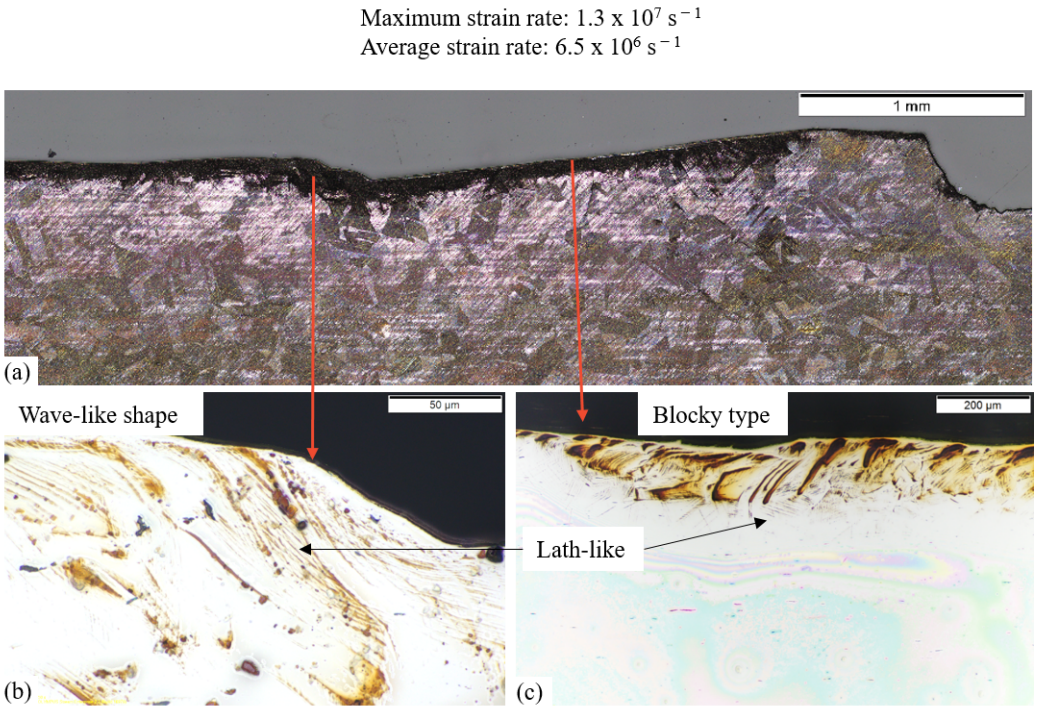

Figure 13. Microstructure analysis of a specimen from a cutting test: (**a**) Beraha II etching, (**b**) magnetic etching, (**c**) blocky martensite in the strongly deformed area directly below the surface and lath-like form at greater depth.

With increasing strain rate, more α'-martensite formed in the subsurface area during the cutting experiments. Furthermore, a more homogeneous layer with less isle formation was present; see Figure 14a,b.

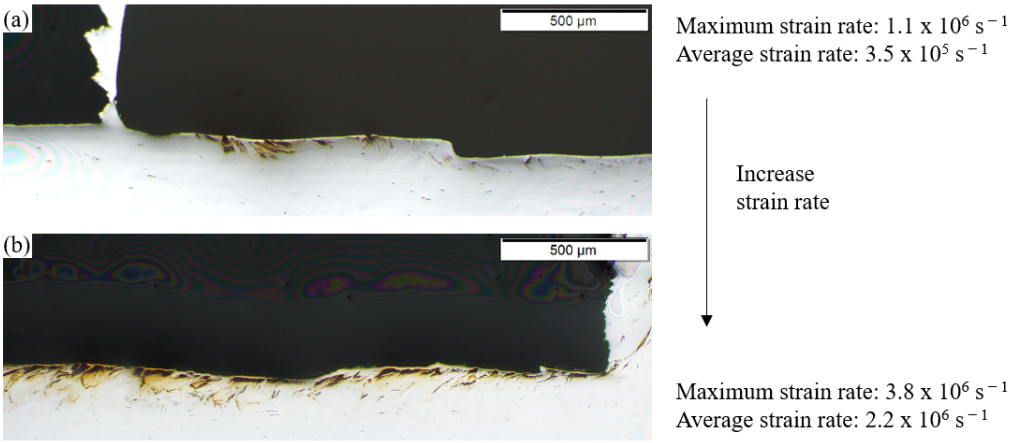

Figure 14. Magnetic etching of specimens from cutting tests at −45 °C: (**a**) lower strain rate, (**b**) higher strain rate.

4. Discussion

Many researchers have found that for non-static tensile tests with increasing strain rate, the formation of martensite is suppressed by adiabatic heating, e.g., [12,14,15,31]. In the present study, this was also observed upon tensile testing. With increasing strain rate, fewer black areas were visible, and thus less martensite was formed. Additionally, these

specimens experienced the highest strain rate at the fracture area [30] and less martensite was formed there, cf. Figure 7. However, no such correlation was found in this study for the other stress states analyzed, namely shear and compression. With increasing strain rate, more martensite was transformed, and thus, as described by Cao et al., the strain rate seems to have a positive influence on the formation of strain-induced martensite [12].

Furthermore, different types of α'-martensite were formed depending on the stress state. Under tensile and shear stress, only lath-like martensite was found in the present study. This corresponds to the nucleation of α'-martensite embryos at shear band intersections and further growth, described as type b nucleation of α'-martensite by [31]. The coalescence for growth occurs outside the slip plane but retains the distinct crystallographic character [31]. The diffraction analysis of Asghari-Rada et al. has shown that the planes with maximum intensity for the α' phase are the planes (110), (200), (211) and (220) [32]. Further, as previously described by [31], the visible growth of the lath-like α'-martensite occurs along the [022] direction in one of the $\{111\}$ slip planes. For compressive deformation, the blocky martensite type was found. This corresponds to the type c described in Ref. [31]. The blocky martensite is formed when many intersections exist. In this case, the intersection nuclei outside the slip plane grow together with the intersection nuclei on the adjacent slip plane. Thereby, the defined crystallographic character remains [31]. Compressive stress suppresses the formation of α'-martensite, as the martensitic transformation is accompanied by an increase in volume [33]. Therefore, other deformation mechanisms, such as dislocation slip or twinning, take place and many intersections occur [31]. This leads to a blocky martensite form.

Looking at the surface of a specimen from a cutting test, blocky martensite near the surface is evident, cf. Figures 13 and 14. This is where most of the deformation takes place and therefore many intersections exist. Compared to the compression specimens, a substantial amount of α'-martensite was formed. Due to the small cutting area, high strain rates (up to two magnitudes higher than in the compression specimens) occurred within the cutting experiment in the same test setup. This leads to an increased martensitic transformation.

In addition, only for this stress condition, a wave-like martensite form was found in this area next to the blocky α'-martensite. As described in [7], the deformation takes place in two slip systems, causing the curvature in the plane trace. These newly created deformation lines act as nucleation sites for the martensite transformation. Thus, transformation into α'-martensite apparently takes place along the deformation track, leading to a wavy structure of the α'-martensite. This is most likely to happen if material is accumulated, resulting in high stresses and high temperatures. In a machining process, this can be a sign of a built-up edge. Here, the cutting edge is altered by the adhesion of the workpiece material to the cutting edge, resulting in an undefined rounding of the newly formed cutting edge. After some time, this material loosens and the original cutting edge breaks free. Due to cold shut, the adhesion of the workpiece material is so strong that the original surface of the tool is also torn out by breaking, leaving an undefined cutting edge. At this moment, the machining process becomes unstable and a rough surface is created, which appears similar to the shoulder shown in Figure 13a.

Moreover, in this highly compressed area, less α'-martensite was formed compared to the rest of the subsurface, cf. Figure 13b,c. Jo et al. described that the occurrence of adiabatic shear bands (ASB) is less likely when the deformed material shows the DIMT effect [34]. However, the emergence of ASB is a well-known structure that forms in various metallic materials during deformation at high strain rates due to thermal–mechanical instability resulting from an abrupt temperature rise, followed by strong plastic flow [34]. Due to the high temperature rise, less α'-martensite was formed in these regions and further investigations should look for the formation of ASB.

With increasing depth, more lath-like α'-martensite can be found in a machined metastable austenitic steel. Less deformation takes place here, and thus there are fewer intersections where α'-martensite nucleation occurs. Moreover, Shrinivas et al. observed

that with increasing strain rate, the lath martensite type changes to the blocky type [35]. According to FEM simulations, the highest strain rate occurs directly at the surface during a machining process. This supports that the change in the martensite form near the surface is due to shear stresses and not compressive stress, which can also produce a blocky α'-martensite form; see Figure 9. This leads to the conclusion that the passive force is not the main driving factor for the creation of martensite in a subsurface zone produced by cryogenic cutting. The passive force mostly produces compressive stresses in a cutting process, whereas the cutting force also leads to shear stresses. Mayer et al. concluded that an increase in the effective passive force leads to an increase in the DIMT [2]. The effective passive force takes into account the passive and the cutting force. The corresponding calculation can be found in Ref. [2]. Due to the results obtained in this study, it can be stated that the shear stresses and not the compression stresses should be increased to obtain a higher martensite transformation rate within a cutting process.

In some samples, non-transformed grains were found; see Figures 10–12. It should be noted that at the surface of these non-transformed grains, lath-like black structures can be found. Using EBSD, no martensite was detected there. Due to the highly deformed surface area, however, it is possible that there is some martensite and it is simply not detectable by EBSD. Nevertheless, these structures indicate that there were two active slip systems. As described in [7], two planes of the {111} family are active in AISI 304 at low temperatures. This indicates that twins are formed even though the SFE is low in the steel used in the present study. Since no martensitic structure appeared in the SEM pictures in these areas—see Figures 11a and 12a—these features are attributed to shear band formation, which is also found in surfaces produced by cryogenic cutting [6,7]. No trend regarding the influence of the strain rate on the formation of non-transformed grains was found. In an actual machining process, however, the tendency for non-transformed grains increases with increasing cutting temperature [7]. In the present study, a change in the deformation mechanism depending on the experimental temperature was found. At 20 °C, the Schmid factor in the Y-direction for $<111> \parallel \{100\}$ for the non-transformed grain was very low. Hence, the force was not sufficient to create martensite. Additionally, considering the GAM in Figure 11c, a subgrain development in the non-transformed grain becomes evident. Thus, dislocation glide was the main deformation mechanism and not the transformation of α'-martensite. This in turn suggests that the cutting temperature must be sufficiently low to suppress dislocation slip and the development of subgrains. Further, the GAM at room temperature is widespread, which shows that there are areas with higher misorientation angles, and thus a high dislocation density. This again needs to be avoided to ensure a homogeneous martensitic transformation.

At −110 °C, the Schmid factor of a non-transformed grain was close to 0.5—see Figure 12a—and thus a martensitic transformation would have been expected to occur. The GAM shows, in addition, a low misorientation angle, cf. Figure 12b. However, directly on the grain boundaries of the non-transformed grain, a high misorientation angle becomes evident. This indicates that a grain rotation took place and the energy was used to rotate the grain and not to convert it into martensite. Here, dislocation slip at the grain boundaries was energetically more favorable.

An IPF analysis showed that at −110 °C, the dislocation movement took place mainly in one plane. Other planes showed almost no dislocation activity. This indicates that the temperature should not be chosen too low so that dislocation movements can take place in other planes as well. However, the lower stacking fault energy due to the temperature decrease seems to be more suited to create martensite than a slightly higher temperature, cf. [7].

Using EBSD, it was not possible to detect a bcc structure because the subsurface was highly deformed. However, it was possible to produce images of the same non-transformed grain with surrounding α'-martensitic structures using different analytical methods. Magnetic etching can make the same martensitic structures visible compared to SEM and EBSD, cf. Figure 10. In case of strongly deformed structures such as the subsurface

analyzed here, it is possible to distinguish α'-martensite from other deformation products with the aid of magnetic etching in contrast to EBSD.

In general, more α'-martensite was formed in the cutting experiments than for the single stress condition experiments. Shrinivas et al. also found that uniaxial tension produces less martensite compared to the multiaxial condition during rolling under similar experimental conditions because multiple slip systems are activated in multiaxial systems [35]. Additionally, the activation of multiple slip systems forms more irregular, blocky martensite [31], which can be observed for specimens machined.

Although the current study has clearly demonstrated the effects of strain rate and stress state on the martensitic transformation, the effect cannot yet be exploited to optimize and tailor the actual cutting process for inducing a certain surface condition in a component. Clearly, this calls for inline monitoring of the martensite evolution and a feedback loop to control the process. Work is currently underway to address this issue.

The more homogeneously the subsurface of a workpiece is transformed to martensite, the better the hardening effect is. Increasing the cutting stress and strain rate leads to less isle formation; therefore, a high feed rate that increases the cutting stress and strain rate should be chosen to achieve a homogeneous hardening effect. However, a low surface quality results from high feed rates.

5. Conclusions

In this study, the influence of different stress states and high strain rates on the deformation-induced α'-martensite transformation was investigated. The following results were obtained.

- With increasing strain rate, the α'-martensite transformation is suppressed under tensile loading. As described in the literature, this can be explained by an increase in adiabatic heating.
- Under shear loading, an increase in deformation-induced α'-martensite was found with increasing strain rate.
- For pure compressive loading, almost no α'-martensite transformation took place.
- Under a multiaxial stress state, which is present at the surface during a machining process, the highest α'-martensite transformation was observed. An increase in the α'-martensite content with increasing strain rate was found.
- Furthermore, under compressive conditions, in multiaxial systems and at high strain rates, a blocky α'-martensite was observed. Under shear stresses and lower strain rates, a lath α'-martensite was found. Since the subsurface of the specimens cut mainly exhibits a blocky α'-martensite and shear stresses support the martensitic transformation more than compressive stresses, the blocky α'-martensite seems to be due to the high strain rates and not due to compressive forces.

Author Contributions: Conceptualization, L.V.F., A.K. and G.G.; methodology, L.V.F. and A.K.; validation, L.V.F., A.K., G.G. and H.J.M.; formal analysis, L.V.F. and A.K.; investigation, L.V.F. and A.K.; writing—original draft preparation, L.V.F.; writing—review and editing, G.G., B.B., H.J.M. and S.B.; visualization, L.V.F.; supervision, S.B.; project administration, S.B.; funding acquisition, H.J.M. and B.B. All authors have read and agreed to the published version of the manuscript.

Funding: This research was funded by the German Research Foundation (DFG) within the research priority program SPP 2086, grant number 401800578. The publication of this article was funded by the Open Access Fund of Leibniz Universität Hannover.

Institutional Review Board Statement: Not applicable.

Informed Consent Statement: Not applicable.

Data Availability Statement: Data are available from the corresponding author upon request.

Acknowledgments: The authors thank A. Krabbenhöft for support with the EBSD analysis.

Conflicts of Interest: The authors declare no conflict of interest.

References

1. Frölich, D.; Magyar, B.; Sauer, B.; Mayer, P.; Kirsch, B.; Aurich, J.; Skorupski, R.; Smaga, M.; Beck, T.; Eifler, D. Investigation of wear resistance of dry and cryogenic turned metastable austenitic steel shafts and dry turned and ground carburized steel shafts in the radial shaft seal ring system. *Wear* **2015**, *328–329*, 123–131. [CrossRef]
2. Mayer, P.; Kirsch, B.; Müller, C.; Hotz, H.; Müller, R.; Becker, S.; von Harbou, E.; Skorupski, R.; Boemke, A.; Smaga, M.; et al. Deformation induced hardening when cryogenic turning. *CIRP J. Manuf. Sci. Technol.* **2018**, *23*, 6–19. [CrossRef]
3. Hotz, H.; Smaga, M.; Kirsch, B.; Zhu, T.; Beck, T.; Aurich, J.C. Characterization of the subsurface properties of metastable austenitic stainless steel AISI 347 manufactured in a two-step turning process. *Procedia CIRP* **2020**, *87*, 35–40. [CrossRef]
4. H.Hotz.; Kirsch, B. Influence of tool properties on thermomechanical load and surface morphology when cryogenically turning metastable austenitic steel AISI 347. *J. Manuf. Process.* **2020**, *52*, 120–131. [CrossRef]
5. Hotz, H.; Kirsch, B.; Becker, S.; von Harbou, E.; Müller, R.; Aurich, J.C. Improving the surface morphology of metastable austenitic steel AISI 347 in a two-step turning process. *Procedia CIRP* **2018**, *71*, 160–165. [CrossRef]
6. Fricke, L.V.; Nguyen, H.N.; Breidenstein, B.; Zaremba, D.; Maier, H.J. Eddy Current Detection of the Martensitic Transformation in AISI304 Induced upon Cryogenic Cutting. *Steel Res. Int.* **2020**, *2*, 2000299. [CrossRef]
7. Fricke, L.V.; Gerstein, G.; Breidenstein, B.; Nguyen, H.N.; Dittrich, M.A.; J., M.H.; Zaremba, D. Deformation-induced martensitic transformation in AISI304 by cryogenic machining. *Mater. Lett.* **2021**, *285*, 129090. [CrossRef]
8. Olson, G.B.; Cohen, M. A mechanism for the strain-induced nucleation of martensitic transformations. *J. Less-Common Met.* **1972**, *28*, 107–118. [CrossRef]
9. Olson, G.B.; Cohen, M. A Perspective on Martensitic Nucleation. *Annu. Rev. Mater. Sci.* **1981**, *11*, 1–32. [CrossRef]
10. Jaspers, S. Metal Cutting Mechanics and Material Behaviour. Ph.D. Thesis, Eindhoven University of Technology, Eindhoven, The Netherlands, 1999. [CrossRef]
11. Krüger, L.; Wolf, S.; Martin, S.; Martin, U.; Jahn, A.; Weiß, A.; Scheller, P. Strain Rate Dependent Flow Stress and Energy Absorption Behaviour of Cast CrMnNi TRIP/TWIP Steels. *Steel Res. Int.* **2011**, *82*, 1087–1093. [CrossRef]
12. Cao, B.; Iwamoto, T.; Bhattacharjee, P.P. An experimental study on strain-induced martensitic transformation behavior in SUS304 austenitic stainless steel during higher strain rate deformation by continuous evaluation of relative magnetic permeability. *Mater. Sci. Eng. A* **2020**, *774*, 138927. [CrossRef]
13. Das, A.; Tarafder, S.; Chakraborti, P.C. Estimation of deformation induced martensite in austenitic stainless steels. *Mater. Sci. Eng. A* **2011**, *529*, 9–20. [CrossRef]
14. Hecker, S.S.; Stout, M.G.; Staudhammer, K.P.; Smith, J.L. Effects of Strain State and Strain Rate on Deformation-Induced Transformation in 304 Stainless Steel: Part I. Magnetic Measurements and Mechanical Behavior. *Metall. Mater. Trans. A* **1982**, *13*, 619–626. [CrossRef]
15. Eckner, R.; Krüger, L.; Motylenko, M.; Savinykh, A.S.; Razorenov, S.V.; Garkushin, G.V. Deformation mechanisms and microplasticity of austenitic TRIP/TWIP steel under flyer plate impact. *Epj Web Conf.* **2018**, *183*, 03007. [CrossRef]
16. Denkena, B.; Tönshoff, H.K. *Spanen–Grundlagen*; Springer: Berlin/Heidelberg, Germany, 2011.
17. Hopkinson, B. A method of measuring the pressure produced in the detonation of high explosives or by the impact of bullets. *Proc. R. Soc. Lond. A* **1914**, *89*, 411–413. [CrossRef]
18. Chen, W.W.; Song, B. *Split Hopkinson (Kolsky) Bar*; Mechanical Engineering Series; Springer: New York, NY, USA, 2011; pp. 7–35. [CrossRef]
19. Gama, B.A.; Lopatnikov, S.L.; Gillespie., J.W. Hopkinson bar experimental technique: A critical review. *Appl. Mech. Rev.* **2004**, *57*, 223–250. [CrossRef]
20. Francis, D.K.; Whittington, W.R.; Lawrimore, W.B.; Allison, P.G.; Turnage, S.A.; Bhattacharyya, J.J. Split Hopkinson Pressure Bar Graphical Analysis Tool. *Exp. Mech.* **2017**, *57*, 179–183. [CrossRef]
21. Larbi, S.; Djebali, S.; Bilek, A. Study of High Speed Machining by Using Split Hopkinson Pressure Bar. *Procedia Eng.* **2015**, *114*, 314–321. [CrossRef]
22. Zhang, Z.; Wang, Z.; Wang, W.; Jiang, R.; Xiong, Y. Investigation on surface quality of high-speed cutting titanium alloy Ti6Al4V based on Split-Hopkinson pressure bar. *Proc. Inst. Mech. Eng. Part B* **2020**, *234*, 1293–1301. [CrossRef]
23. Berkovic, L.; Chabotier, A.; Coghe, F.; Rabet, L. Measuring and modeling of low temperature Hopkinson tests. *Procedia Eng.* **2011**, *10*, 1645–1650. [CrossRef]
24. Merklein, M.; Biasutti, M. Forward and Reverse Simple Shear Test Experiments for Material Modeling in Forming Simulations. In Proceedings of the 10th International Conference on Technology of Plasticity, ICTP 2011, Aachen, Germany, 25–30 September 2011; pp. 702–707.
25. Olson, G.B.; Cohen, M. Kinetics of strain-induced martensitic nucleation. *Metall. Trans. A* **1975**, *6*, 791. [CrossRef]
26. Gray, R.J. Magnetic Etching with Ferrofluid. In *Metallographic Specimen Preparation: Optical and Electron Microscopy*; McCall, J.L., Mueller, W.M., Eds.; Springer: Boston, MA, USA, 1974; pp. 155–177. [CrossRef]
27. Talonen, J.; Aspegren, P.; Hänninen, H. Comparison of different methods for measuring strain induced α-martensite content in austenitic steels. *Mater. Sci. Technol.* **2004**, *20*, 1506–1512. [CrossRef]
28. Schuhmann, H. Zur Metallographie der $\gamma \rightarrow \epsilon \rightarrow \alpha$ - Umwandlung in hochlegierten Stählen. *Prakt. Metallogr.* **1967**, *4*, 265–283.
29. Celada-Casero, C.; Kooiker, H.; Groen, M.; Post, J.; San-Martin, D. In-Situ Investigation of Strain-Induced Martensitic Transformation Kinetics in an Austenitic Stainless Steel by Inductive Measurements. *Metals* **2017**, *7*, 271. [CrossRef]

30. Lee, W.S.; Lin, C.F. Morphologies and characteristics of impact-induced martensite in 304L stainless steel. *Scr. Mater.* **2000**, *43*, 777–782. [CrossRef]
31. Murr., L.E.; Staudhammer, K.P.; Hecker, S.S. Effects of Strain State and Strain Rate on Deformation-Induced Transformation in 304 Stainless Steel: Part II. Microstructural Study. *Metall. Mater. Trans. A* **1982**, *13*, 627–635. [CrossRef]
32. Asghari-Rad, P.; Shirazi, H.; Koldorf, S.; Nili-Ahmadabadi, M. Microstructure evolution of an Austenitic Stainless Steel severely deformed by the repetitive corrugation and straightening by rolling and subsequent annealing. In Proceedings of the 5th International Biennial Conference on Ultrafine Grained and Nanostructured Materials, Tehran, Iran, 11–12 November 2015; pp. 1–8.
33. Totten, G.E. (Ed.) *Steel Heat Treatment: Metallurgy and Technologies*, 2nd ed.; CRC Taylor & Francis: Boca Raton, FL, USA, 2007.
34. Jo, M.C.; Kim, S.; Suh, D.W.; Hong, S.S.; Kim, H.K.; Sohn, S.S.; Sunghak. Role of retained austenite on adiabatic shear band formation during high strain rate loading in high-strength bainitic steels. *Mater. Sci. Eng. A* **2020**, *778*, 139118. [CrossRef]
35. Shrinivas, V.; Varma, S.K.; Murr, L.E. Deformation-induced martensitic characteristics in 304 and 316 stainless steels during room-temperature rolling. *Metall. Mater. Trans. A* **1995**, *26*, 661–671. [CrossRef]